Research Square

Preprints are preliminary reports that have not undergone peer review.
They should not be considered conclusive, used to inform clinical practice,
or referenced by the media as validated information.

Volatile depletion in rocky planets is a chemical fingerprint of hybrid accretion

Haiyang Wang

haiyang.wang@sund.ku.dk

University of Copenhagen https://orcid.org/0000-0001-8618-3343

Anders Johansen

Center for Star and Planet Formation, GLOBE Institute, University of Copenhagen, Denmark
https://orcid.org/0000-0002-5893-6165

Ziyan Xu

University of Copenhagen

Marie-Luise Steinmeyer

ETH Zurich

Michiel Lambrechts

University of Copenhagen https://orcid.org/0000-0001-9321-5198

Elishevah van Kooten

University of Copenhagen https://orcid.org/0000-0003-3333-4421

Chao-Chin Yang

The University of Alabama https://orcid.org/0000-0003-2589-5034

Zhaohuan Zhu

University of Nevada, Las Vegas https://orcid.org/0000-0003-3616-6822

Dante Lauretta

University of Arizona https://orcid.org/0000-0002-2597-5950

Martin Bizzarro

University of Copenhagen https://orcid.org/0000-0001-9966-2124

Article

Keywords:

Posted Date: May 15th, 2026

DOI: https://doi.org/10.21203/rs.3.rs-8195443/v1

License: This work is licensed under a Creative Commons Attribution 4.0 International License.
Read Full License

Additional Declarations: There is **NO** Competing Interest.

Volatile depletion in rocky planets is a chemical fingerprint of hybrid accretion

Haiyang S. Wang[1*], Anders Johansen[1*], Ziyan Xu[1], Marie-Luise Steinmeyer[2], Michiel Lambrechts[1], Elishevah van Kooten[1], Chao-Chin Yang[3], Zhaohuan Zhu[4], Dante S. Lauretta[1,5], Martin Bizzarro[1]

[1*]Center for Star and Planet Formation, Globe Institute, University of Copenhagen, 1350 Copenhagen, Denmark.
[2]Institute for Particle Physics and Astrophysics, ETH Zürich, 8093 Zürich, Switzerland.
[3]Department of Physics and Astronomy, University of Alabama, Tuscaloosa, AL 35487-0324, USA.
[4]Department of Physics and Astronomy and Nevada Center for Astrophysics, University of Nevada, Las Vegas, NV 89154-4002, USA.
[5]Lunar and Planetary Laboratory, University of Arizona, Tucson, AZ85721, USA.

*Corresponding author(s). E-mail(s): haiyang.wang@sund.ku.dk; anders.johansen@sund.ku.dk;

Abstract

Volatile depletion in rocky planets relative to their host stars is commonplace in both the Solar System and exoplanetary systems, yet the connections between planet formation and composition remain elusive. Here we model devolatilization during pebble accretion in combination with collisional growth from volatile-depleted planetesimals to explore the formation pathways of Earth and Mars. Using Bayesian inference, we find that bulk silicate Earth is best reproduced by $\gtrsim$75% contribution from two protoplanets formed via pebble accretion, supplemented by up to $\sim$25% material from planetesimals that are compositionally akin to the asteroid Vesta. Using instead a planetesimal volatile-depletion curve that is not observed among known meteorite parent bodies would allow the planetesimal contribution to reach $\mathbf{40^{+15}_{-14}}$%. In comparison, bulk silicate Mars reflects

27±5% pebble-accreted material and 73±5% Vesta-like planetesimals. We identify volatile depletion as a chemical fingerprint of hybrid accretion, in which both pebble accretion and collisional assembly contribute to terrestrial planet growth. By quantitatively linking formation pathways to volatile budgets, our findings demonstrate how planetary accretion histories can be inferred from elemental signatures, with broad implications for interpreting the chemical diversity of rocky exoplanets.

The compositions of the inner Solar System planets Earth and Mars show as a common feature that their mantle abundances of moderately volatile lithophile elements (MVLEs) are depleted relative to the proto-Sun ([1–3]; Fig. 1). MVLEs are defined as elements with condensation/sublimation temperatures lower than those of the major rock-forming elements Mg and Si but higher than those of atmophile species such as H_2O, and that preferentially remain in the silicate mantle during core-mantle differentiation. This common "devolatilization" feature of MVLEs [4, 5] has been attributed to several processes. These include (i) incomplete condensation during an early, ultra-hot stage of the solar protoplanetary disk [6–8], (ii) melting and partial evaporation of planetesimals driven by radiogenic heating and/or collisional kinetic energy [9–11], and (iii) partial vaporization of protoplanets by giant impacts [12, 13]. Importantly, devolatilization in rocky planet formation may be a universal process [4]. Support for this hypothesis comes from the inferred compositions of rocky exoplanetary material, based on spectroscopic measurements of polluted white dwarf atmospheres [14, 15] and wide-binary/co-moving stars with signatures of planet ingestion [16, 17].

Anchored by MVLE depletions in both Earth and Mars, we probe here potential formation pathways of terrestrial planets, which remain highly debated [18, 19], particularly between rapid pebble accretion [20, 21] and prolonged mutual collisions of planetesimals and protoplanets [22, 23]. Our goal is not to contrast these two competing theories, but to assess the viability of a potential *hybrid scenario*. This scenario is motivated by simulations showing that both pebble accretion and mutual collisions have the potential to drive planetary growth in the inner regions of protoplanetary disks where rocky planets form [24]. If several processes indeed contribute to the assembly of rocky planets, then those processes must imprint various signatures in the volatile depletion of terrestrial planets, based on which the relative contributions of these processes can be retrieved.

A high ambient temperature during the formation of planetary building blocks in the protoplanetary disk is often assumed to explain the depletion of MVLEs in Earth [6–8]. However, in the emerging disk wind paradigm for protoplanetary disks, mass accretion through the disk is mainly facilitated through winds launched by large-scale magnetic fields [25, 26]. The temperature increase of the disk caused by wind-driven accretion is far lower than in the traditional model of turbulence-driven accretion, with a mid-plane temperature remaining $\lesssim$ 300 K at 1 au [27]. Indeed, the presence of moderately volatile siderophile elements (MVSEs), along with carbon and oxygen, in iron meteorites also point to the formation of even the earliest planetesimal generations under such cool conditions [28–31]. Further, sample returns from the asteroids Ryugu

and Bennu (Fig. 1) demonstrate that dust similar in composition to CI chondrites – pristine and solar-like, except for the most volatile elements (H, C, N and noble gases) – was widespread in the Solar System [32, 33].

Alternatively, melting and evaporation of early-formed planetesimals has been suggested as a viable mechanism of volatile loss, caused by the decay of short-lived radionuclides (e.g., ^{26}Al and ^{60}Fe, [9, 34]) and/or energetic planetesimal collisions [10, 11, 31]. Meteorites from the differentiated asteroid Vesta, a body sometimes categorized as a surviving planetary embryo [35], show strong depletion of elements with sublimation temperatures below ∼1200 K [7, 36](Fig. 1). It is not understood whether Vesta's depletion of volatile elements is due to high ambient disk temperatures [7] or evaporation from a magma ocean [37], and some volatile elements may even have become stored in the core during differentiation of Vesta [38]. Here we adopt the view that Vesta represents a population of early-formed planetesimals that degassed their lithophile volatiles before contributing to the accretion of Earth and Mars (we will assess the effect of potentially volatile-bearing core material [31] separately). We note that the angrite meteorite group shows an even stronger elemental depletion than meteorites from Vesta, being depleted even in Si and Mg [39]; this provides additional support for melting as a widespread mechanism of volatile loss of early-formed planetesimals.

On the other hand, thermal processing of pebbles during their accretion, which is typically not considered in previous work [7, 10, 18], offers a new mechanism for impoverishing volatiles [20, 40, 41]. Here we use a 1-D model of the gas envelope of a protoplanet undergoing pebble accretion [20, 40] to calculate the loss of MVLEs through thermal processing of pebbles as they descend through the H_2/He-dominated gaseous envelope (Methods). Figure 2a shows the cumulative sublimation fraction of both refractory and volatile lithophile elements over the growth of a protoplanet. When the sublimation temperature of a volatile lithophile ($T_{\rm sub}$; Methods; Extended Data Table 1) is lower than the temperature at the bottom of the envelope ($T_{\rm env}$; Extended Data Fig. 1), the element is assumed to sublimate and subsequently escape into the disk through envelope convection. Importantly, this mass loss does not apply to refractory species (Si and Mg and more refractory); these elements sublimate instead into a deep silicate vapor atmosphere in equilibrium with the underlying magma ocean, protected from diffusion to the upper envelope by an inner radiative zone where silicate cloud formation strongly inhibits the convection [40, 42].

To validate our assumption of complete loss of a volatile element once it has been sublimated into the envelope, we perform 3-D hydrodynamical simulations of the convective flow pattern in the envelope (Fig. 2b; Methods). Within the convective zone (distance from the planet surface $R \lesssim R_{\rm B}$, where $R_{\rm B}$ is the Bondi radius), the released volatiles are transported upward by convective mixing. Upon reaching the recycling region ($R \gtrsim R_{\rm cyc}$), they are carried away by large-scale recycling flows from the protoplanetary disk that penetrate the Hill sphere, and they are thus lost from the envelope [43, 44]. Figure 2b presents the temporal evolution of volatiles in the envelope (assuming $R_{\rm cyc} = 2R_{\rm B}$). Within 1 year, only ∼30% of the volatiles remain in the envelope, and only $\lesssim$3% remain by 5 years. This is consistent with a diffusion timescale of ∼1 year measured from the velocity dispersion of the particles (Extended Data Fig. 2a). Our

assumption of $R_{\rm cyc} = 2R_{\rm B}$ is conservative, as previous simulations indicate that $R_{\rm cyc}$ is likely close to $R_{\rm B}$ [43], reducing the diffusion timescale to ∼0.1–1 years (Extended Data Fig. 2b). Recent simulations of envelope convection coupled realistically to the gas flow from the protoplanetary disc [43, 44] show that the tracer particles in a fully convective envelope will indeed be depleted within a timescale of a couple of years [44]. Notably, efficient escape applies to volatiles both in the gas phase and recondensed into (or onto) grains of sizes $\lesssim$10 μm, which are well-coupled to the gas and do not sediment appreciably towards the protoplanet [45]. Even under the extreme assumption that volatiles would recondense onto sedimenting pebble-sized particles (mm-cm, [45]), these volatiles would simply go on to sublimate again deep in the envelope and be more likely to condense onto μm-sized grains (due to the higher total surface of such small grains) at their next upwards passage across their sublimation temperature.

Results

Here we show the results of our evaluation of the viability of a potential *hybrid scenario* – in which rocky planets grow by a combination of pebble accretion, planetesimal accretion, and giant impacts – against the bulk silicate (lithophile) compositions of Earth and Mars ([2, 3]; Supplementary Table 1) by applying both a reduced-χ^2 minimization and a Bayesian inference framework (Methods).

A hybrid pathway of Earth formation

For Earth (Fig. 3), we consider formation primarily from a three-component mixture: the proto-Earth (**PE**) and one (giant) impactor (**Imp**) – both of which grew via pebble accretion (and subject to devolatilization during the process) – along with early-formed planetesimals (**Plm**) that are assumed to have a Vesta-like composition (Methods). We have also examined a series of alternative scenarios: in particular, including *or not* a population of volatile-depleted (Vesta-like) and/or volatile-rich (CI-like) planetesimals, accretion of pebbles that are volatile-poor, as well as varying the number of impactors onto our proto-Earth (Table 1, column 1). We note that EH chondrites from the inner Solar System have CI-like levels of MVLEs (Fig. 1), but we will nevertheless for simplicity of notation refer to our pristine, non-depleted planetesimal component as 'CI-like'.

We start with a reduced-χ^2 minimization approach to explore the plausible parameter space for the primary three-component scenario (**PE+Plm+Imp**) by setting up a grid of the relative mass fractions of those three components (in terms of planetesimal mass fraction, $f_{\rm Plm}$, and the mass ratio of impactor to proto-Earth, r_M, shown in the 2D space as in Fig. 3b). The minimum of the reduced-χ^2 (χ^2/N, where $N = 13$ is the number of lithophile elements considered in the fit: Al, Ti, Ca, Cr, Mg, Si, Li, Mn, Na, K, F, Zn, and In) is 3.3. Within an increase of χ^2/N of unity from the minimum value, a large range of solutions for both r_M (0.1–1.0) and $f_{\rm Plm}$ (0–0.4) can be achieved.

We then employ Bayesian inference with dynamical nested sampling, along with a set of reasonable priors (Methods; Extended Data Table 2), to place probabilistic constraints on the parameter estimation of a series of proposed models. The test results

based on (logarithmic) Bayesian evidence ($\ln Z$) and Bayes factor ($\Delta \ln Z$) suggest that the models **PE+Plm+Imp** and **PE+Imp** perform equally well in explaining the data (Table 1; Fig. 4a; Supplementary Fig. 3a). By comparing the volatility trends produced with these two models (Fig. 3a and Extended Data Fig. 3a) and the resulting reduced-χ^2 values (3.3 vs. 3.6; Table 1, column 3), we find that the **Plm** component particularly contributes to a better explanation of the lithium level, which is elevated in Earth relative to **PE+Imp**. The **PE+Imp+Plm** and **PE+Imp** models together inform a hybrid accretion pathway of Earth's formation that requires at least ∼75% mass contribution from proto-Earth and an impactor formed via pebble accretion, with up to ∼25% from the Vesta-like planetesimal component (Table 1, column 2).

We go on to test the essentiality of including the pebble-grown **PE** and **Imp** components and we also introduce a volatile-rich CI-like planetesimal population (**CI**) (Extended Data Fig. 3b–e). Without an **Imp**, the **PE+Plm** model is disfavored (relative to the reference **PE+Plm+Imp** model) at the 'substantial' level according to Jeffreys' scale ([46, 47]; Methods) that measures the strength of Bayesian evidence ($\Delta \ln Z = -1.31 \pm 0.07$, Table 1, column 5). Without including any pebble-grown body, the **CI+Plm** model is disfavored 'decisively' ($\Delta \ln Z = -11.31 \pm 0.07$). By re-adding one or both of the pebble-grown bodies, the **PE+CI+Plm** and **PE+CI+Plm+Imp** models return higher $\Delta \ln Z$ values of -2.07 ± 0.07 and -1.78 ± 0.08, respectively, while remaining disfavored 'substantially' relative to the reference **PE+Plm+Imp** model. The contribution of a CI-like population of planetesimals is nevertheless no more than 10% $M_\oplus$ (within 1σ uncertainty; Table 1, column 2) in these models.

We have also quantified the range of the mass fraction of an impactor in the two favored **PE+Plm+Imp** and **PE+Imp** models: 8–43% $M_\oplus$ (within 1σ uncertainty; Table 1, column 2). This relatively large range is in line with the canonical Moon-forming giant impact (Theia) mass (∼10–15% $M_\oplus$; [48, 49]) and also the range required for Theia (∼28–46% $M_\oplus$) to disrupt a primordial resonant chain evolving into the present-day configuration of the inner Solar System [50]. The possibility of multiple impactors has also been tested in the **PE+Plm+DualImp** (with dual impactors) and **PE+Plm+TriImp** (with triple impactors) models (Extended Data Fig. 4). The dual-impactor scenario is plausible (given its $|\Delta \ln Z| < 1$), as long as the mass of the secondary impactor is low ($0.04^{+0.08}_{-0.03} M_\oplus$), with its posterior distribution skewing towards the lower end of the mass range (Supplementary Fig. 4). The triple-impactor scenario is evidently disfavored (with $\Delta \ln Z = -1.77 \pm 0.07$), and the mass of the third impactor (even if it exists) would be negligible ($0.01^{+0.02}_{-0.01} M_\oplus$). The number of giant impacts preferred in our model is thus somewhat below the mean number of giant impacts seen in N-body simulations (∼3, [51]); the inclusion of pebble accretion in terrestrial planet formation naturally implies that fewer planetesimal seeds are required to form terrestrial-mass planets, resulting in fewer protoplanets and hence fewer giant impacts.

As an alternative to accreting pebbles of solar-like composition, our tests for volatile-poor pebbles are constructed by scaling the levels of pre-depletion of pebbles relative to that of H chondrites (Methods). We find that the reduced-χ^2 of the best fit increases as a function of the increasing pre-depletion factor (Extended Data Fig. 5a) while the relative contributions from **PE**, **Plm** and **Imp** remain similar. This

demonstrates that pre-depletion of accreted pebbles gives a poorer fit to the volatile depletion of Earth (Extended Data Fig. 5b–d), even if pre-depleted pebbles cannot be excluded based on Bayesian evidence (with $|\Delta \ln Z| \lesssim 1$). Such volatile-depleted pebbles could nevertheless have contributed to the later stages of proto-Earth's growth (beyond $\sim 0.15 M_\oplus$; Fig. 2a) where all moderately volatile elements would be anyway lost during the accretion.

A hybrid pathway of Mars formation

For Mars, we consider its growth through a combination of pebbles and planetesimals accreted within the protoplanetary disk lifetime, motivated by its inferred rapid core formation [52]. Our reference model, based on Bayesian inference, consists of 27±5 % by mass via pebble accretion (**PM**) and 73±5 % by mass from planetesimals with a Vesta-like composition (**Plm**) (Figs. 4b and 5; Table 1). This finding is in line with silicon isotope constraints on Mars' accretion that suggest significant contribution from material akin to Vesta-like planetesimals [53].

For alternative scenarios of Mars' accretion, we have primarily focused on varying the volatile-depletion levels of the accreted planetesimals. As done for Earth, we first introduce a population of volatile-rich CI-like planetesimals as a replacement of the pebble-grown component **PM** (forming the planetesimal-mixture model of **CI+Plm**) and as an addition to the existing components (constituting the **PM+CI+Plm** model). The **CI+Plm** model is disfavored 'strongly' (with $\Delta \ln Z = -4.11 \pm 0.06$), with a worsening fit towards Zn and In in particular (Extended Data Fig. 6a). The addition of a pebble-grown component in the **PM+CI+Plm** model elevates the Bayes factor to -2.37 ± 0.09, but it remains disfavored 'substantially' due to the (unnecessary) model complexity (Extended Data Fig. 6b). The contribution of a CI-like planetesimal population to Mars' final mass remains well below 10% ($0.03^{+0.04}_{-0.02} M_{\rm Mars}$). Similar as for Earth, this lands somewhat below a previously proposed accretion of 10-15% CI-like material contribution to Earth [5]. Considering pre-depleted pebbles for Mars yields a **PM** contribution that increases by about 10%, but also leads to poorer overall fits to the volatile depletion of Mars (Supplementary Fig. 2).

We then go on to test hypothetical planetesimal populations with varied volatile-depletion scales by modulating the two variables of the logistic model for volatile-depleted planetesimals (Eq. 1; Methods; also see ref. [7])): the inflection point (T_0) and the steepness parameter (σ_0). We first apply the reduced-χ^2 minimization in a parameter space of varied T_0 ([900, 1600] K) and $f_{\rm Plm}$ ([0.1, 1.0]) (Fig. 5b). The result indicates a confined region – $T_0 \sim$ 1100–1400 K and $f_{\rm Plm} \sim$ 60–80% – where χ^2/N values are comparably small. Our further Bayesian inference (Extended Data Fig. 7a) returns a quantitative value of $T_0 = 1363^{+43}_{-52}$ K and $f_{\rm Plm} = 68 \pm 5$ % (corresponding to the star sign with error bars in orange in Fig. 5b; refer to Table 1 for model details). This implies that an unidentified type of planetesimals with moderately volatile elements even more depleted than Vesta could have contributed to forming Mars.

We further test the steepness parameter σ_0 (together with T_0) of the planetesimal logistic model in a wide range of 10–500 K (indicating an extended mixture of various volatile-depleted planetesimals) in the case of Mars (Extended Data Fig. 7b). The result with the highest Bayesian evidence shows $T_0 = 1273^{+70}_{-65}$ K and $\sigma_0 = 227^{+78}_{-75}$,

representing the respective, *average* properties of various populations of hypothetical planetesimals. Correspondingly, the total fraction of this mixture is 79^{+11}_{-9}%, leaving the remaining 21^{+9}_{-11}% to be via pebble accretion (Table 1, column 2). In all of these tested cases for Mars, the mass contribution from early-formed planetesimals is unanimously dominant, over ~65%, while the contribution from pebble accretion is never less than 10% (within 1σ uncertainty), reinforcing the hybrid-accretion nature of Mars formation.

Similar tests done for Earth by freeing the assumption of Vesta-like planetesimals (Methods; Supplementary Figs. 7–9) further solidify the hybrid-accretion nature of Earth formation, with a dominant contribution from two protoplanets grown by pebble accretion. The contribution of such a hypothetical population of planetesimals could reach 40^{+15}_{-14}%, when we optimize the composition of the early-formed planetesimals without considering any potential devolatilization of Mg, Si, and Cr of the pebbles before or during pebble accretion (Methods). Taken together, these results suggest that Earth experienced a relatively high pebble accretion rate while Mars's pebble accretion remained comparably sluggish – possibly due to gravitational stirring of its orbit by other, more massive protoplanets [54].

Discussion

The efficiency of impact-driven devolatilization of planetesimals and protoplanets depends on both impact speed and the mass of the target body [13, 55–57]. For the specific case of K loss, ref. [57] found collisional devolatilization to be only relevant for planetary bodies up to about Moon mass. Beyond that, insufficient energy is available for vapor to escape from the deep gravitational potential. This upper limit around Moon mass is interesting, since protoplanets of higher mass reach the MVLE devolatilization domain driven by pebble sublimation (Fig. 2a), while radiogenic heating and/or collisional devolatilization may have been responsible for volatile loss on planetesimals and smaller protoplanets [9, 31]. We nevertheless emphasize that collisional devolatilization from impacts during the disk phase is still poorly understood [58], as the disk gas may facilitate vapor loss.

Our hybrid-accretion models based on MVLEs also carry important implications for the abundances of MVSEs. Unlike MVLEs, those MVSEs are potentially preserved in planetesimal cores. Indeed, non-carbonaceous (NC) iron meteorites, which sample the cores of early-formed planetesimals in the inner solar system, record MVSE-rich compositions [31]. Here, we focus on sulfur (S) given its MVSE nature and that it is a major light element candidate in the cores of both Earth and Mars [2, 59, 60]. We have adopted an approximate range of the CI-normalized abundance of S in iron meteorite parent bodies (~0.1–1; [31]) to represent the S abundance in the Vesta-like planetesimals (**Plm**). Based on the best solutions of our reference models (**PE+Plm+Imp** and **PM+Plm**; Table 1), we estimate the protosolar-normalized ranges of S abundance in bulk Earth and Mars: 0.10–0.23 and 0.19–0.85, respectively (Extended Data Fig. 8). These ranges are consistent with the recent (and higher) estimate of S content in Earth's core [59] and with constraints on Mars' core based on seismic data [61],

instead of the traditional (and lower) estimates of S content in the terrestrial planets' cores based on BSE/BSM's volatility trends [2, 3, 60, 62].

Our reference model (**PE+Plm+Imp**) of Earth's hybrid accretion aligns well with a recent three-component model [63] developed to explain the relatively low excess of ^{182}W in Earth's mantle. W is siderophile, but ^{182}W is continuously created in the mantle by decay of ^{182}Hf with a half-life of 8.9 million years. The model of [63] invokes 20% contribution from planetesimals and 80% contribution from two protoplanets of mass 0.7 $M_{\rm E}$ and 0.1 $M_{\rm E}$, respectively, both formed via pebble accretion. If this view is correct, then the low ^{182}W excess measured for our planet reflects the ongoing delivery of metal to Earth's core – segregating in the process W from the mantle – by planetesimal accretion as well as in the Moon-forming giant impact [64].

Based on isotopic compositions, there is an ongoing debate about whether Earth and Mars formed from purely inner Solar System materials or had significant isotopic contribution from pebbles drifting in from the outer Solar System [18, 21]. While the composition of Earth lies on a mixing line between inner-solar-system ureilites and outer-solar-system CI-chondrites in the isotopic distribution of many major elements such as Si and Ca [21], Earth appears as an endmember in other elements such as Mo and Zr [22]. The latter has been interpreted as evidence that Earth formed from a lost reservoir of planetesimals [22] or otherwise that Earth lost an isotopically distinct component embedded in FeS/CaS/MgS grains [53] and in water ice [20, 65] when these components were subject to sublimation during pebble accretion. Our thermal processing model for pebbles, which underpins the hybrid accretion of Earth, aligns well with the latter view. Our composition-based results, complementary to isotopic analyses that remain debated [18, 21, 22, 53, 65, 66], help refine the range of viable formation pathways for Earth and Mars.

The loss of volatile elements during the accretion of Earth and Mars carries significant implications for the source of life-essential volatile elements (e.g., C, H, N, O, P, and S) on rocky planets. Those elements are expected to be substantially depleted during the pebble accretion phase, even if the protoplanet grows in the region just exterior to the water ice line [20, 67]. Volatile delivery to rocky planets thus occurs both through the direct accretion of volatile-rich pebbles – before the protoplanet reaches the sublimation temperature of the relevant volatile – and through impacts with smaller protoplanets. Additionally, accretion of primitive planetesimals, which formed late enough to avoid substantial devolatilization, could further contribute to the volatile budget [5, 68]. Extending these results to rocky planets around other stars, the observed depletion of moderately volatile elements in the spectra of both Sun-like and evolved stars – suspected to have recently accreted rocky planetary materials [15, 17] – suggests that volatile loss is a universal process. Understanding the volatile loss process thus provides an important context for evaluating the compositional diversity and potential habitability of rocky exoplanets.

Methods

Bulk (silicate) compositions of Earth and Mars

We have selected the major rock-forming lithophile elements (Mg, Si, Cr, Al, Ca, Ti, Mn, Na, K, and Zn), supplemented by a few of less abundant but thermally relevant lithophiles (Li, F, In, Cl, Br, and I) to cover a wide range of elemental volatility. We adopt the composition of bulk silicate Earth (i.e., Earth excluding its core) for those lithophiles from [2], which is calibrated from various geophysical, geochemical, and cosmochemical models [69–71]. We note that the more recent estimates of bulk silicate Earth composition for these selected lithophiles [72] are consistent with our adopted composition (within uncertainties). For the composition of bulk silicate Mars (i.e., Mars excluding its core), we adopt the estimates from ref. [3] for the same list of lithophiles as above. The more recent estimates (but for fewer lithophiles) for Mars from ref. [60] are found to be consistent with the adopted estimates [3], except for Mn, Na, and Zn (these newer estimates are also indicated in Fig. 5). We have checked that if we had instead adopted these estimates of Mn, K, and Zn, then that does not change our best-inferred models. We refer to Supplementary Table 1 for the protosolar [4] and Al-normalized composition of those selected major rock-forming lithophile elements.

The abundances of heavy halogens (Cl, Br, and I) in CI chondrites were revised downward in [73], resulting in significantly higher values in the CI-normalized compositions of bulk silicate Earth and Mars (shown in light blue in Figs. 3 and 5). However, this downward revision has been put into question due to the use of a limited sample for the measurement as well as large inconsistency with previous measurements of various CI chondritic samples [74, 75]. It has also been suggested that since heavy halogens are highly incompatible during partial melting, their strong depletion on Earth may result from preferential loss through collisional erosion [76]. For these reasons, we have chosen to exclude Cl, Br and I from our quantification of the best models, but we show both sets of estimates for comparison in Figs. 3 and 5.

The abundances of some lithophiles suspected of slight siderophile or chalcophile tendencies, specifically Cr, Mn, and Zn, may not represent volatile depletions in bulk planets. See Supplementary Information for our abundance correction for these three elements and the sensitivity test by excluding them (Supplementary Fig. 1).

Pressure-dependent elemental sublimation temperature

Elemental volatility is essential to understanding volatile depletion, and it is pressure-dependent. We therefore need to compute the ambient pressure that pebbles experience within the envelope during pebble accretion. Although envelope pressures vary from the top to bottom of the envelope, it is the bottom pressure that is the highest and also determines whether materials falling into the envelope would be eventually accreted onto the growing planet or experience sublimation before accretion. Hence, we employ the envelope bottom pressures ($P_{\rm env}$) (as well as temperature $T_{\rm env}$) that are calculated over the growth of an Earth-mass planet with a 1-D envelope model of pebble accretion described below.

Based on the pressure-dependent calculations of 50% condensation temperatures of elements (T_c^{50}; [8]) for a solar-composition gas that is equivalent to our H_2/He-dominated envelope gas, we interpolate the T_c^{50}, as a proxy for T_{sub} in chemical equilibrium (see further discussion in Supplementary Information), for the specific pressure at which an element starts to sublimate and which is found where the pressure-dependent T_c^{50} crosses the P_{env}–T_{env} profiles for different disk opacity conditions (as described below and Extended Data Fig. 1). We find that the T_{sub} values for an element as adopted here between the upper and lower limits of the opacity conditions are nearly identical (with the largest difference of ∼20 K for In; Extended Data Table 1). It is therefore reliable to adopt the mean of the T_{sub} values (with negligible error bars) within the range of opacity conditions as the proxy for elemental volatility for further model exploration. There is a small, systematic difference of ∼5 K in T_{sub} between values calculated for the plausible disk conditions at the locations of Earth and Mars. This small systematic shift of elemental volatility does not influence our model parameter exploration and thus is discarded for simplicity.

1-D envelope model of pebble accretion

The 1-D model used to calculate the P_{env}–T_{env} profile at the bottom of the envelope (Fig. 2a and Extended Data Fig. 1) is based on analytical derivations described in detail in ref. [77]. The outer boundary P–T conditions are given at the Hill radius $R_H = [M_p/(3M_\odot)]^{1/3} r$ – where M_p is the planetary mass, $M_\odot$ is the stellar mass and r is the distance of the planet from the star – with the relevant conditions in the protoplanetary disk at 1 au ($T_\oplus \approx 120\,K$ and $P_\oplus \approx 0.2\,Pa$). The depth of the radiative-convective boundary (RCB), below which energy is transported purely by convection, depends on the luminosity of the planet and the opacity of the gas. We calculate the planet luminosity, assuming planetary growth with an e-folding timescale of $\tau_{acc} = 0.7\,Myr$, as $L_p = GM_p\dot{M}_p/R_p$, where $\dot{M}_p$ is the mass accretion rate (M_p/τ_{acc}) and R_p is the radius of the protoplanet. The opacity in the envelope is given by $\kappa = \kappa_d(T_{env}/T_{disk})^2$, where $T_{disk} = T_\oplus(r/au)^{-3/7}$ [78] and $\kappa_d = [0.1, 1]\,m^2\,kg^{-1}$ are the temperature and opacity conditions in the surrounding protoplanetary disk, with the opacity arising mainly from sub-micron-sized dust grains as in ref. [77]. Knowing the temperature and pressure at the RCB, we then construct an adiabatic solution for the convective envelope – with mean molecular weight and adiabatic index from a solar mixture of H_2 and He – down to its bottom (that is in touch with the surface of the planet). The metallicity and opacity of the envelope gas could be increased from dust and recondensed MLVEs released from the infalling pebbles [79]. We have experimented with our model by increasing the opacity parameter κ_d by a factor of 3 (and even higher) over the unity value. The resultant P_{env}–T_{env} profile does not change significantly (Extended Data Fig. 1), due to the nearly-adiabatic temperature profile. The T_{sub} values of elements only weakly depend on pressure (Extended Data Fig. 1), so a small increase in metallicity will only increase those values monotonically and limited to a few of tens of K [80, 81]. Therefore, we do not expect it will affect our results and conclusions. We have also experimented with higher values of the ambient disk temperature, to represent conditions interior to the water ice line, and found similar results.

Following previous work [40, 42], we assume that an inner radiative zone (IRZ) emerges following the rapid building-up of a SiO-dominated vapor at the innermost envelope, where $T_{\rm env}$ reaches the sublimation temperature ($\gtrsim$ 1450 K; Extended Data Table 1) of silicates in accreted pebbles at the conditions of the innermost envelope. This IRZ (i.e., the saturated SiO-dominated cloud layer) prevents sublimated refractory materials (Si, Mg, as well as more refractory elements) from diffusing to the upper envelope and hence from loss by the recycling flow [43, 44, 82]. Before pebbles reach the IRZ, they will have already sublimated their MVLEs including Li and Mn (with $T_{\rm sub} \lesssim$ 1320 K; Extended Data Table 1). Given this physical separation between the sublimation of the moderately volatile elements and the IRZ, we adopt a characteristic temperature ∼1400 K to represent the transition between MVLEs (thermally processed and diffused in the envelope) and refractory elements (protected by the IRZ). This results in the jump in the volatile-depletion curve between moderately volatile Li and Mn and refractory Mg and Si in the Earth (Fig. 3a).

We nevertheless caution that loss of moderately refractory elements (Si, Mg and Cr) is physically plausible if early-accreted pebbles experience some degree of sublimative mass loss before a protective IRZ builds up [40, 42], since 10–20% depletion of this group of elements has been found in the terrestrial planet [4, 83] as well as in potentially rocky exoplanetary materials inferred from polluted white dwarfs [15]. Our pebble-devolatilization model is not yet precise enough to capture this transient regime. Alternatively, such a depletion may also be explained by accretion of more volatile-depleted planetesimals (like angrite parent bodies [39]). We further discuss the effect of inclusion/exclusion of this group of elements on our model-fitting outcome in Supplementary Information.

3-D convection simulations in the envelope

We perform 3-D hydrodynamical simulations of a convective gas envelope (Fig. 2b) using the `Athena++` magnetohydrodynamic code [84], which uses a high-order Godunov scheme for solving the fluid dynamics. Volatiles released in the envelope are treated as passive particles that move with the local velocity of the gas. These particles are implemented using the Lagrangian tracer particles module based on the particle-mesh method [85, 86]. When studying the volatile loss process, particles that cross the convection-recycling boundary $R_{\rm cyc}$ are manually removed to mimic the recycling flow. This approach allows us to explore volatile loss across different values of $R_{\rm cyc}$ (and thus varied diffusion timescales; Extended Data Fig. 2).

Our setup generally follows the "isolated spherical envelope" case of ref. [87], where convection is driven by accretion heating, which is distributed throughout the envelope to follow a prescribed pebble accretion luminosity profile $(1 - R_{\rm in}/R)L_{\rm p}$, where $R_{\rm in}$ is the inner boundary radius of the simulation. $L_{\rm p}$ is again the planet luminosity, which can be calculated with the mass accretion timescale $\tau_{\rm acc}$. Instead of radiative cooling assumed in ref. [87], we adopt Newtonian cooling, which damps the gas temperature beyond $R_{\rm B}$ to the ambient disk temperature $T_{\rm disk}$ on a cooling timescale of 0.16 years, which is on the order of the disk dynamical timescale. Since the convective envelope is typically optically thick around 1 au region [44], radiative cooling is negligible, making this approach a reasonable and computationally efficient approximation of the

cooling process. We confirm its robustness by verifying that the thermal structure and flow velocity patterns in the envelope remain consistent with simulations using full radiative transfer.

Our simulations consider the envelope around a planet of mass $M_{\rm p} = M_{\oplus}$, located at 1 au from a solar-mass star. We note that the convection speed is not expected to vary much as a function of planet mass (from $0.1M_{\oplus}$ to $3M_{\oplus}$; [88]). The ambient disk temperature at 1 au is set to be $T_{\rm disk} \approx 250\,{\rm K}$ and the midplane gas density is set as $\approx 10^{-9}\,{\rm g\,cm^{-3}}$. The pebble accretion luminosity is determined by an accretion timescale of $\tau_{\rm acc} = 10^6\,{\rm yr}$. We note that this disk temperature is higher than that assumed in the 1-D model, and the accretion timescale is slightly longer than in the 1-D model. However, these descrepancies are not expected to significantly impact the results. If any effect occurs, our adopted higher disk temperature and longer accretion timescale likely result in weaker convection, thus lowering volatile loss efficiency, which makes our results a conservative estimate. Our simulation domain covers from $R_{\rm in} = 7R_{\oplus} (= 0.1R_{\rm B})$ to $R_{\rm out} = 2111R_{\oplus} (= 30R_{\rm B})$, with 140 radial grid cells uniformly distributed in logarithmic space. The domain is discretized with 160 cells on the azimuthal direction and 40 cells on the poloidal direction. This ensures that the convective flow, with a characteristic lengthscale of $R_{\rm B}$, is well-resolved. Our simulations incorporate a total number of $\sim 9 \times 10^5$ tracer particles, providing robust statistic sampling of the volatile dynamics.

Volatile-depleted planetesimal model

In our assumption of a volatile-depleted planetesimal model, we have adopted the lithophile composition of Vesta [36] and a logistic curve of volatile depletion fit for it with $T_{\rm c}^{50}$ of those lithophiles referred at the canonical pressure of 10^{-4} bar [7]. However, to include the composition trend of Vesta (i.e. retaining the similar volatile depletion levels) in our model parameter exploration self-consistently, we have re-fit a logistic curve to the protosolar-normalized Vesta lithophile composition (f) as a function of $T_{\rm sub}$ of those lithophiles (Extended Data Table 1). This yields a set of $T_{\rm sub}$-adapted inflection point ($T_0 = 1135 \pm 35$ K) and steepness parameter ($\sigma_0 = 62 \pm 24$ K) of the Vesta logistic model used in this work,

$$f = \frac{1}{2}\left[1 + {\rm erf}\left(\frac{T_{\rm sub} - T_0}{\sigma_0\sqrt{2}}\right)\right], \tag{1}$$

where erf is the Gauss error function, related to the cumulative distribution of a normal distribution. These values are nevertheless consistent with those ($T_0 = 1081 \pm 29$ K and $\sigma_0 = 57 \pm 17$ K) of ref. [7], in which they interpret these two parameters respectively as the nominal mid-plane temperature and width/extension of the feeding zone where the objects formed/accreted. The equivalent effect on volatile depletion of early-formed planetesimals has also been attributed to short-lived radiogenic heating (e.g., by ^{26}Al and ^{60}Fe; [9]) or to planetesimal collisions [10, 11, 31]. Here, we are agnostic of the exact pathway(s) through which early-formed planetesimals are thermally processed. We choose to adopt the $T_{\rm sub}$-adapted Vesta-like logistic curve above as the baseline model for volatile-depleted planetesimals, while we also adjust T_0 and

σ_0 broadly to extend this Vesta-specific logistic model to a hypothetical, collective model of volatile-depleted planetesimals and thus examine their effects on the accretion of both Earth and Mars. At an extreme case where both T_0 and σ_0 are set to near zero, the logistic function would mimic compositionally CI-like (non-volatile-depleted) planetesimals. In addition, we also test further in Supplementary Information (i) an alternative, exponential model for Vesta-like planetesimals (Supplementary Fig. 9a): $\log_{10}(f) = b(\frac{T_0' - T_{\rm sub}}{T_0'})$, where constants $b = -5.78 \pm 0.18$ and $T_0' = 1284 \pm 4$ – the latter representing the kink point between the slope (depletion) and the horizontal line (i.e., non-depletion); (ii) a scenario without a model fit to the Vesta (HED meteoritic) data (Supplementary Fig. 9b).

Pre-depletion model of accreted pebbles

We test plausible levels of pre-depletion in the accreted pebbles by scaling the composition of the pebbles in MVLEs between proto-solar composition and H-type ordinary chondrite composition (H-chondrites are one of the most volatile-depleted chondrite groups in the inner protoplanetary disk [89]). To do so, we first fit a common exponential model to the H-chondrite composition f relative to Al and proto-Sun,

$$\log_{10} f = b^{\rm H} \cdot \frac{T_0^{\rm H} - T_{\rm sub}}{T_0^{\rm H}}\,, \tag{2}$$

where $T_0^{\rm H}$ describes the temperature below which the H-chondrites are volatile-depleted (we assume solar composition above this threshold temperature) and $b^{\rm H}$ describes the steepness of the depletion. We find $b^{\rm H} = -3.12$ and $T_0^{\rm H} = 997$ K for the H-chondrite depletion model. Different levels of pre-depletion (b) of accreted pebbles are then scaled to $b^{\rm H}$ – namely, $b = [0, 1]b^{\rm H}$, while fixing at $T_0^{\rm H}$. We note that alternative models such as polynomial and power-law forms could also be fit to H chondrite data, but they are all consistent with one another within the uncertainties of the fits [59]. Since here we only use the H-chondrite model as baseline for scaling various levels of volatile pre-depletion in pebbles, the exact form and its uncertainty is not important. For a broader discussion of pre-depleted pebbles, we refer to the Supplementary Information.

Model parameter estimation

Reduced-χ^2 minimization

To assess the fit between the modeled and observed lithophile element abundances, we first employ a reduced chi-squared (χ^2) minimization approach. For each element, we compare the observed value to the model prediction at the corresponding temperature or composition by identifying the closest match in the model grid of relative fractions of different components – pebble-accreting bodies (protoplanet and impactor) and Vesta-like planetesimals. The χ^2 contribution for each element is computed in linear space. Asymmetric data uncertainties are conservatively handled by adopting the larger of the upper and lower bounds. The total χ^2 is then summed across all elements for fitting and normalized by the degrees of freedom (equivalent

to the number of fit elements, N) to yield the reduced statistic (χ^2/N). This metric provides a first-order quantitative measure of the goodness-of-fit. We have also made an alternative computation of χ^2/N in the logarithmic space and found that the solutions agree with those found in the linear space.

Probabilistic inference via Bayesian nested sampling

To quantify the compositional contributions of various planetary building blocks, we also employ a Bayesian inference framework using nested sampling via the `dynasty` Python package, specifically employing its dynamic nested sampling mode. This approach allows for efficient exploration of complex posterior distributions and simultaneous estimation of the Bayesian evidence. Compared to traditional Markov Chain Monte Carlo (MCMC) methods, nested sampling is particularly advantageous for problems involving multi-modal posteriors, strong parameter correlations, or pronounced degeneracies [90] – all of which are relevant to the inference problem addressed here. A set of priors (Extended Data Table 2) are applied to perform the Bayesian inference. The initial values of three parameters controlling the dynamic sampling efficiency and stop criteria are set moderately: `nlive_init`=600, `nlive_batch`=300, and `dlogz`=0.05, which are kept the same for all cases.

Based on the posterior distributions of the Bayesian inference, the [16th, 50th, 84th] percentiles of individual model parameters are calculated and taken as the summary of the parameter space (Table 1). To report the strength of Bayesian evidence for model comparison, we adopt the following criteria of Jeffreys' scale [46, 47] on the absolute Bayes factor ($|\Delta \ln Z|$):

0–1 'Not worth mentioning (insignificant)'
1–2.5 'Substantial'
2.5–5 'Strong'
$> \mathbf{5}$ 'Decisive'

For clarity in describing whether a model is disfavored or not relative to the reference models, the true (instead of absolute) value of a Bayes factor is often used, while the strength of Bayesian evidence is measured against the criteria above.

Data availability

All data supporting the findings of this study are available within the paper and its Supplementary Information.

Code availability

The codes essential to reproduce the work are available on CodeOcean upon the publication of this work.

References

[1] Albarède, F. Volatile accretion history of the terrestrial planets and dynamic implications. Nature **461**, 1227–1233 (2009).

[2] Wang, H. S., Lineweaver, C. H. & Ireland, T. R. The elemental abundances (with uncertainties) of the most Earth-like planet. Icarus **299**, 460–474 (2018).

[3] Yoshizaki, T. & McDonough, W. F. The composition of Mars. Geochimica et Cosmochimica Acta **273**, 137–162 (2020).

[4] Wang, H. S., Lineweaver, C. H. & Ireland, T. R. The volatility trend of protosolar and terrestrial elemental abundances. Icarus 287–305 (2019).

[5] Braukmüller, N., Wombacher, F., Funk, C. & Münker, C. Earth's volatile element depletion pattern inherited from a carbonaceous chondrite-like source. Nature Geoscience **12**, 564–568 (2019).

[6] Bond, J. C., O'Brien, D. P. & Lauretta, D. S. The compositional diversity of extrasolar terrestrial planets. i. in situ simulations. The Astrophysical Journal **715**, 1050–1070 (2010).

[7] Sossi, P. A., Stotz, I. L., Jacobson, S. A., Morbidelli, A. & O'Neill, H. S. C. Stochastic accretion of the Earth. Nature Astronomy 951–960 (2022).

[8] Lodders, K., Fegley, B., Mezger, K. & Ebel, D. Condensation and the volatility trend of the earth. Space Science Reviews **221**, 54 (2025).

[9] Eatson, J. W., Lichtenberg, T., Parker, R. J. & Gerya, T. V. Devolatilization of extrasolar planetesimals by 60fe and 26al heating. Monthly Notices of the Royal Astronomical Society **528**, 6619–6630 (2024).

[10] Hin, R. C. et al. Magnesium isotope evidence that accretional vapour loss shapes planetary compositions. Nature **549**, 511–515 (2017).

[11] Halliday, A. & Porcelli, D. In search of lost planets – the paleocosmochemistry of the inner solar system. Earth and Planetary Science Letters **192**, 545–559 (2001).

[12] Norris, C. A. & Wood, B. J. Earth's volatile contents established by melting and vaporization. Nature **549**, 507–510 (2017).

[13] Saurety, A., Caracas, R. & Raymond, S. N. Impact-induced vaporization during accretion of planetary bodies. The Astrophysical Journal Letters **981**, L13 (2025).

[14] Harrison, J. H., Shorttle, O. & Bonsor, A. Evidence for post-nebula volatilisation in an exo-planetary body. Earth and Planetary Science Letters **554**, 116694 (2021).

[15] Aguilera-Gómez, C. et al. Host star and exoplanet composition: Polluted white dwarf reveals depletion of moderately refractory elements in planetary material. Astronomy and Astrophysics **693**, A64 (2025).

[16] Galarza, J. Y., López-Valdivia, R., Meléndez, J. & Lorenzo-Oliveira, D. Evidence of Rocky Planet Engulfment in the Wide Binary System HIP 71726/HIP 71737. The Astrophysical Journal **922**, 129 (2021).

[17] Liu, F. et al. At least one in a dozen stars shows evidence of planetary ingestion. Nature **627**, 501–504 (2024).

[18] Morbidelli, A., Kleine, T. & Nimmo, F. Did the terrestrial planets of the solar system form by pebble accretion? Earth and Planetary Science Letters **650**, 119120 (2025).

[19] Johansen, A., Olson, P. & Sharp, Z. Comment on "Did the terrestrial planets of the Solar System form by pebble accretion?". Preprint at arXiv:2411.17043 (2024).

[20] Johansen, A. et al. A pebble accretion model for the formation of the terrestrial planets in the solar system. Science Advances **7**, 1–14 (2021).

[21] Bizzarro, M., Johansen, A. & Dorn, C. The cosmochemistry of planetary systems. Nature Reviews Chemistry **9**, 378–396 (2025).

[22] Burkhardt, C. et al. Terrestrial planet formation from lost inner solar system material. Science Advances **7**, eabj7601 (2021).

[23] Morbidelli, A. et al. Contemporary formation of early Solar System planetesimals at two distinct radial locations. Nature Astronomy **6**, 72–79 (2022).

[24] Lambrechts, M. et al. Formation of planetary systems by pebble accretion and migration. How the radial pebble flux determines a terrestrial-planet or super-Earth growth mode. Astronomy and Astrophysics **627**, A83 (2019).

[25] Béthune, W., Lesur, G. & Ferreira, J. Global simulations of protoplanetary disks with net magnetic flux. I. Non-ideal MHD case. Astronomy and Astrophysics **600**, A75 (2017).

[26] Lesur, G. et al. Inutsuka, S., Aikawa, Y., Muto, T., Tomida, K. & Tamura, M. (eds) Hydro-, Magnetohydro-, and Dust-Gas Dynamics of Protoplanetary Disks. (eds Inutsuka, S., Aikawa, Y., Muto, T., Tomida, K. & Tamura, M.) Protostars and Planets VII, Vol. 534 of Astronomical Society of the Pacific Conference Series, 465 (2023).

[27] Mori, S., Okuzumi, S., Kunitomo, M. & Bai, X.-N. Evolution of the Water Snow Line in Magnetically Accreting Protoplanetary Disks. The Astrophysical Journal **916**, 72 (2021).

[28] Grewal, D. S., Dasgupta, R. & Marty, B. A very early origin of isotopically distinct nitrogen in inner solar system protoplanets. Nature Astronomy **5**, 356–364 (2021).

[29] Grewal, D. S., Seales, J. D. & Dasgupta, R. Internal or external magma oceans in the earliest protoplanets – perspectives from nitrogen and carbon fractionation. Earth and Planetary Science Letters **598**, 117847 (2022).

[30] Grewal, D. S., Nie, N. X., Zhang, B., Izidoro, A. & Asimow, P. D. Accretion of the earliest inner Solar System planetesimals beyond the water snowline. Nature Astronomy **8**, 290–297 (2024).

[31] Grewal, D. S., Bhattacharjee, S., Zhang, B., Nie, N. X. & Miyazaki, Y. Enrichment of moderately volatile elements in first-generation planetesimals of the inner Solar System. Science Advances **11**, eadq7848 (2025).

[32] Nakamura, E. et al. On the origin and evolution of the asteroid ryugu: A comprehensive geochemical perspective. Proceedings of the Japan Academy Series B: Physical and Biological Sciences **98**, 227–282 (2022).

[33] Lauretta, D. S. et al. Asteroid (101955) bennu in the laboratory: Properties of the sample collected by osiris-rex. Meteoritics and Planetary Science **59**, 2453–2486 (2024).

[34] Lichtenberg, T., Golabek, G. J., Gerya, T. V. & Meyer, M. R. The effects of short-lived radionuclides and porosity on the early thermo-mechanical evolution of planetesimals. Icarus **274**, 350–365 (2016).

[35] Russell, C. T. et al. Dawn at Vesta: Testing the Protoplanetary Paradigm. Science **336**, 684 (2012).

[36] Mittlefehldt, D. W. Asteroid (4) vesta: I. the howardite-eucrite-diogenite (hed) clan of meteorites. Chemie der Erde **75**, 155–183 (2015).

[37] Fang, L. et al. The origin of 4-Vesta's volatile depletion revealed by the zinc isotopic composition of diogenites. Science Advances **10**, eadl1007 (2024).

[38] Steenstra, E. S. et al. Depletion of potassium and sodium in mantles of Mars, Moon and Vesta by core formation. Scientific Reports **8**, 7053 (2018).

[39] Hu, Y., Moynier, F. & Bizzarro, M. Potassium isotope heterogeneity in the early Solar System controlled by extensive evaporation and partial recondensation. Nature Communications **13**, 7669 (2022).

[40] Steinmeyer, M.-L., Woitke, P. & Johansen, A. Sublimation of refractory minerals in the gas envelopes of accreting rocky planets. Astronomy Astrophysics **181**, 1–16 (2023).

[41] Garai, S., Olson, P. L. & Sharp, Z. D. Building earth with pebbles made of chondritic components. Geochimica et Cosmochimica Acta **390**, 86–104 (2025).

[42] Habib, N. & Pierrehumbert, R. T. Modeling Noncondensing Compositional Convection for Applications to Super-Earth and Sub-Neptune Atmospheres. The Astrophysical Journal **961**, 35 (2024).

[43] Kurokawa, H. & Tanigawa, T. Suppression of atmospheric recycling of planets embedded in a protoplanetary disc by buoyancy barrierc. Monthly Notices of the Royal Astronomical Society **479**, 635–648 (2018).

[44] Kuwahara, A. & Lambrechts, M. Interior dynamics of envelopes around disk-embedded planets. Astronomy and Astrophysics **707** (2026).

[45] Popovas, A., Nordlund, Å., Ramsey, J. P. & Ormel, C. W. Pebble dynamics and accretion on to rocky planets - I. Adiabatic and convective models. Monthly Notices of the Royal Astronomical Society **479**, 5136–5156 (2018).

[46] Jeffreys, H. Theory of Probability Oxford Classic Texts in the Physical Sciences (Oxford University Press, Oxford, 1998). 3rd Edition (First published 1939).

[47] Trotta, R. Bayes in the sky: Bayesian inference and model selection in cosmology. Contemporary Physics **49**, 71–104 (2008).

[48] Canup, R. M. & Asphaug, E. Origin of the moon in a giant impact near the end of the earth's formation. Nature **412**, 708–712 (2001).

[49] Gabriel, T. S. & Cambioni, S. The role of giant impacts in planet formation. Annual Review of Earth and Planetary Sciences **51**, 671–695 (2023).

[50] Huang, S., Ormel, C. W., Zwart, S. P., Kokubo, E. & Yi, T. A resonant beginning for the solar system's terrestrial planets. The Astrophysical Journal **988**, 137 (2025).

[51] Quintana, E. V., Barclay, T., Borucki, W. J., Rowe, J. F. & Chambers, J. E. The Frequency of Giant Impacts on Earth-like Worlds. **821**, 126 (2016).

[52] Dauphas, N. & Pourmand, A. Hf-W-Th evidence for rapid growth of Mars and its status as a planetary embryo. Nature **473**, 489–492 (2011).

[53] Onyett, I. J. et al. Silicon isotope constraints on terrestrial planet accretion. Nature **619**, 539–544 (2023).

[54] Levison, H. F., Kretke, K. A. & Duncan, M. J. Growing the gas-giant planets by the gradual accumulation of pebbles. Nature **524**, 322–324 (2015).

[55] Nakajima, M. & Stevenson, D. J. Melting and mixing states of the earth's mantle after the moon-forming impact. Earth and Planetary Science Letters **427**, 286–295 (2015).

[56] de Vries, J. et al. Impact-induced melting during accretion of the earth. Progress in Earth and Planetary Science **3**, 7 (2016).

[57] Calogero, M. A., Nimmo, F. & Hin, R. C. Can impact-induced heating drive moderately volatile element loss? Earth and Planetary Science Letters **669** (2025).

[58] Kominami, J. & Ida, S. The Effect of Tidal Interaction with a Gas Disk on Formation of Terrestrial Planets. **157**, 43–56 (2002).

[59] Fischer, R. A. & McDonough, W. F. Earth's core composition and core formation, Vol. 1, 17–71 (Elsevier, 2025).

[60] Khan, A., Sossi, P. A., Liebske, C., Rivoldini, A. & Giardini, D. Geophysical and cosmochemical evidence for a volatile-rich mars. Earth and Planetary Science Letters **578**, 117330 (2022).

[61] Stähler, S. C. et al. Seismic detection of the martian core. Science **373**, 443–448 (2021).

[62] McDonough, W. Compositional Model for the Earth's Core, Vol. 3, 559–577 (Elsevier, 2014), 2 edn.

[63] Olson, P. L. & Sharp, Z. D. Hafnium-tungsten evolution with pebble accretion during Earth formation. Earth and Planetary Science Letters **622**, 118418 (2023).

[64] Yu, G. & Jacobsen, S. B. Fast accretion of the Earth with a late Moon-forming giant impact. Proceedings of the National Academy of Science **108**, 17604–17609 (2011).

[65] Bizzarro, M. et al. Interstellar ices as carriers of supernova material to the early solar system. Nature Communications **16** (2025).

[66] Sossi, P. A. & Bower, D. J. Homogeneous accretion of the earth in the inner solar system. Nature Astronomy (2026).

[67] Houge, A. et al. Burned to ashes: How the thermal decomposition of refractory organics in the inner protoplanetary disc impacts the gas-phase c/o ratio. Astronomy & Astrophysics **699**, A227 (2025).

[68] Raymond, S. N., O'Brien, D. P., Morbidelli, A. & Kaib, N. A. Building the terrestrial planets: Constrained accretion in the inner Solar System. Icarus **203**, 644–662 (2009).

[69] Lyubetskaya, T. & Korenaga, J. Chemical composition of earth's primitive mantle and its variance: 1. method and results. Journal of Geophysical Research: Solid Earth **112**, 1–21 (2007).

[70] McDonough, W. F. & Arevalo, R. Uncertainties in the composition of earth, its core and silicate sphere. Journal of Physics: Conference Series **136**, 022006 (2008).

[71] Palme, H. & O'Neill, H. in *Cosmochemical Estimates of Mantle Composition* 2 edn, (ed.Carlson, R. W.) Treatise on Geochemistry 1–39 (Elsevier, 2014).

[72] McDonough, W. F. Earth's composition: Origin, energy budget, and insights from geoneutrinos. Geochimica et Cosmochimica Acta (2025).

[73] Clay, P. L. et al. Halogens in chondritic meteorites and terrestrial accretion. Nature **551**, 614–618 (2017).

[74] Palme, H. & Zipfel, J. The composition of ci chondrites and their contents of chlorine and bromine: Results from instrumental neutron activation analysis. Meteoritics and Planetary Science **17**, 1–17 (2021).

[75] Lodders, K. & Fegley, B. Solar system abundances and condensation temperatures of the halogens fluorine, chlorine, bromine, and iodine. Geochemistry **83**, 125957 (2023).

[76] Campbell, I. H. & O'Neill, H. S. C. Evidence against a chondritic earth. Nature **483**, 553–558 (2012).

[77] Piso, A.-M. A. & Youdin, A. N. On the Minimum Core Mass for Giant Planet Formation at Wide Separations. The Astrophysical Journal **786**, 21 (2014).

[78] Ida, S., Guillot, T. & Morbidelli, A. The radial dependence of pebble accretion rates: A source of diversity in planetary systems. I. Analytical formulation. **591**, A72 (2016).

[79] Brouwers, M. G. & Ormel, C. W. How planets grow by pebble accretion. Astronomy & Astrophysics **634**, A15 (2020).

[80] Timmermann, A., Shan, Y., Reiners, A. & Pack, A. Revisiting equilibrium condensation and rocky planet compositions. Introducing the ECCOplanets code. Astronomy Astrophysics **52** (2023).

[81] Zaveri, U., Wang, H. S. & Sossi, P. A. A chemical perspective on planet formation in reduced systems. Astronomy & Astrophysics, in press (2026).

[82] Wang, Y., Ormel, C. W., Huang, P. & Kuiper, R. Atmospheric recycling of volatiles by pebble-accreting planets. Monthly Notices of the Royal Astronomical Society **523**, 6186–6207 (2023).

[83] Wang, H. S. et al. Enhanced constraints on the interior composition and structure of terrestrial exoplanets. Monthly Notices of the Royal Astronomical Society **482**, 2222–2233 (2019).

[84] Stone, J. M., Tomida, K., White, C. J. & Felker, K. G. The Athena++ Adaptive Mesh Refinement Framework: Design and Magnetohydrodynamic Solvers. The Astrophysical Journal Supplement Series **249**, 4 (2020).

[85] Hu, X., Li, Z.-Y., Zhu, Z. & Yang, C.-C. Formation of dust rings and gaps in non-ideal mhd discs through meridional gas flows. Monthly Notices of the Royal Astronomical Society **516**, 2006–2022 (2022).

[86] Baronett, S. A., Yang, C.-C. & Zhu, Z. Dust–gas dynamics driven by the streaming instability with various pressure gradients. Monthly Notices of the Royal Astronomical Society **529**, 275–295 (2024).

[87] Zhu, Z. et al. Global 3D radiation hydrodynamic simulations of proto-Jupiter's convective envelope. Monthly Notices of the Royal Astronomical Society **508**, 453–474 (2021).

[88] Johansen, A. & Åke Nordlund. Transport, destruction, and growth of pebbles in the gas envelope of a protoplanet. The Astrophysical Journal **903**, 102 (2020).

[89] Lodders, K. Relative atomic solar system abundances, mass fractions, and atomic masses of the elements and their isotopes, composition of the solar photosphere, and compositions of the major chondritic meteorite groups. Space Science Reviews **217**, 44 (2021).

[90] Skilling, J. Nested sampling for general bayesian computation. Bayesian Analysis **1**, 833–860 (2006).

Acknowledgements

We thank B. Fegley and K. Lodders for discussing pressure-dependent condensation temperatures, H. St.C. O'Neill, W. F. McDonough, and P. A. Sossi for Earth and Mars compositions, and Y. Tian for Bayesian inference principles. H.S.W, A.J., Z.X. were supported by the Carlsberg Foundation's Semper Ardens grant ('FIRSTATMO'). C.C.Y. acknowledges the support from NASA via the Emerging Worlds program (#80NSSC23K0653), the Astrophysics Theory Program (#80NSSC24K0133), and the Theoretical and Computational Astrophysical Networks (#80NSSC21K0497). Z.Z. acknowledges support from NASA XRP grant (#80NSSC25K7144). D.S.L. acknowledges support from the Kephalos Research Fund.

Author contributions

Conceptualization, H.S.W, A.J.; Methodology, H.S.W, A.J., M.L.S., Z.X., C.C.Y, Z.Z; Formal Analysis, H.S.W., A.J., Z.X.; Visualization, H.S.W., Z.X.; Validation, all authors; Writing – original draft, H.S.W, A.J., Z.X.; Writing – review & editing, all authors.

Competing interests

The authors declare no competing interest.

Additional information

Extended data is available for this paper at [placeholder]

Supplementary information The online version contains supplementary material available at [placeholder]

Correspondence and requests for materials should be addressed to Haiyang S. Wang and Anders Johansen.

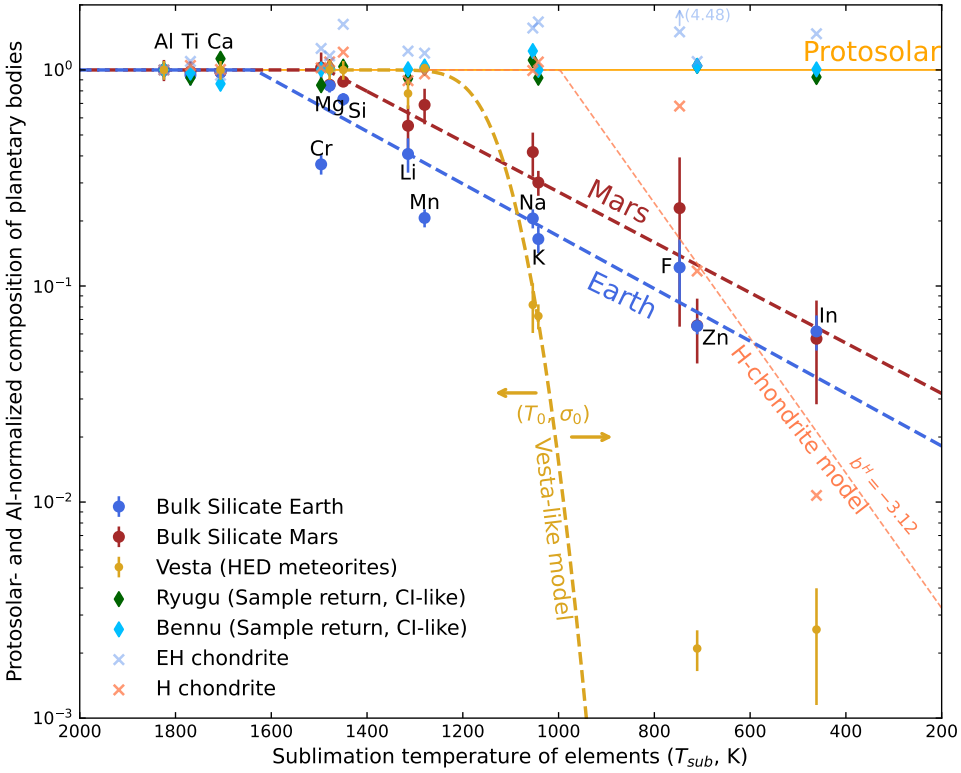


Fig. 1: **Lithophile element compositions of Solar System rocky bodies as a function of elemental volatility.** Protosolar- and Al-normalized composition of major rock-forming lithophile elements in bulk silicate Earth [2], bulk silicate Mars [3], the asteroid Vesta (based on howardite–eucrite–diogenite, HED, meteorites [36]), two asteroid sample returns (Ryugu [32] and Bennu [33]), as well as EH and H chondrites [89] (Supplementary Table 1) are sorted as a function of elemental sublimation temperature (proxy for elemental volatility; Extended Data Table 1). The protosolar composition (normalized as ≡1; [4]) is denoted by the horizontal solid line (orange). The volatile-depletion trends for Earth and Mars (dashed lines in blue and red, respectively) are illustrative only. A logistic function with two variables (T_0 and σ_0, see Eq. 1) recommended in ref. [7] is used to fit the composition of Vesta as a function of $T_{\rm sub}$ (yellow dashed line, for details see Methods). The apparent deviations of Zn and In from the Vesta curve likely caused by their recondensation [37]. The dash line in red indicates an exponential model of H chondrites (with its slope $b^H = -3.12$; Eq. 2), based on which various degrees of volatile pre-depletion in pebbles are scaled (Methods).

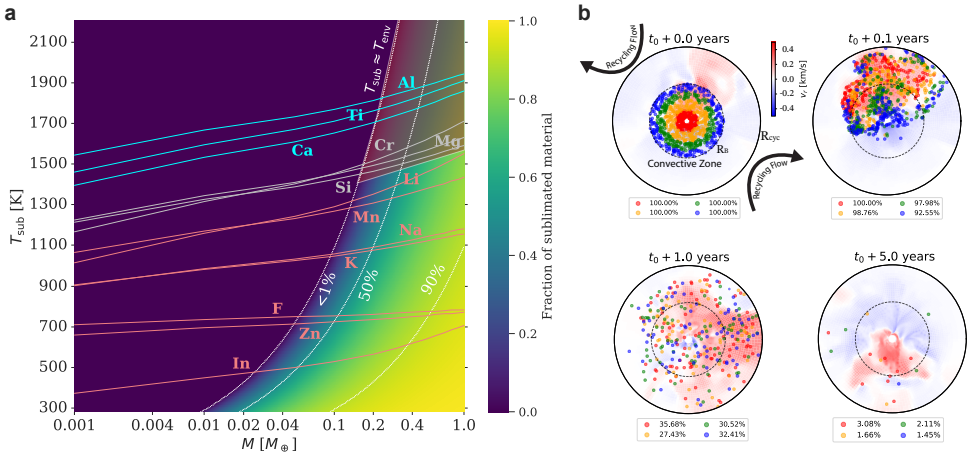


Fig. 2: **Devolatilization during pebble accretion**. (**a**) Sublimation of major rock-forming lithophile elements in the envelope of a protoplanet that grows through pebble accretion. The color map represents the cumulative fraction of sublimated material as a function of the mass of the protoplanet (M, relative to 1 Earth mass, $M_\oplus$) and elemental sublimation temperature ($T_{\rm sub}$), with the '<1%', '50%', and '90%' fractions shown in dotted curves for guidance. The colored lines indicate $T_{\rm sub}$ for selected elements. For moderately volatile lithophiles (red: Li, Mn, Na, K, F, Zn, In), their sublimation and loss back to the protoplanetary disk is assumed to be 100% efficient after their $T_{\rm sub}$ is overtaken by the temperature at the bottom of the envelope ($T_{\rm env}$; along the '<1%' dotted curve; Methods). Major refractory lithophiles (light blue: Al, Ti, and Ca) and moderately refractory lithophiles (gray: Mg, Si and Cr), even if sublimated, are assumed to be retained as vapor in equilibrium with the surface magma ocean, protected from loss by a radiative zone in the silicate cloud layer (indicated by a shadow in light brown on the top right of the panel).(**b**) 3-D hydrodynamical simulations of the temporal evolution of embedded particles (representing sublimated materials) in the convective envelope of a protoplanet during pebble accretion. Particles are initially placed in the spatial intervals 0.1-0.3 $R_{\rm B}$ (red), 0.3-0.6 $R_{\rm B}$ (yellow), 0.6-0.8 $R_{\rm B}$ (green), and 0.8-1 $R_{\rm B}$ (blue) (top-left panel in **b**), where $R_{\rm B}$ is the Bondi radius (indicated by a dashed circle), beyond which the temperature is damped to that of the ambient disk and convection thus suppressed. The transition to the recycling region $R_{\rm cyc}$, where particles escape back to the protoplanetary disk, is assumed to be at $2R_{\rm B}$. The gas radial velocity $v_{\rm r}$ in the envelope is illustrated with red and blue indicating upward and downward flows, respectively. The embedded particles have largely vanished by five years after their release (bottom-right panel in **b**).

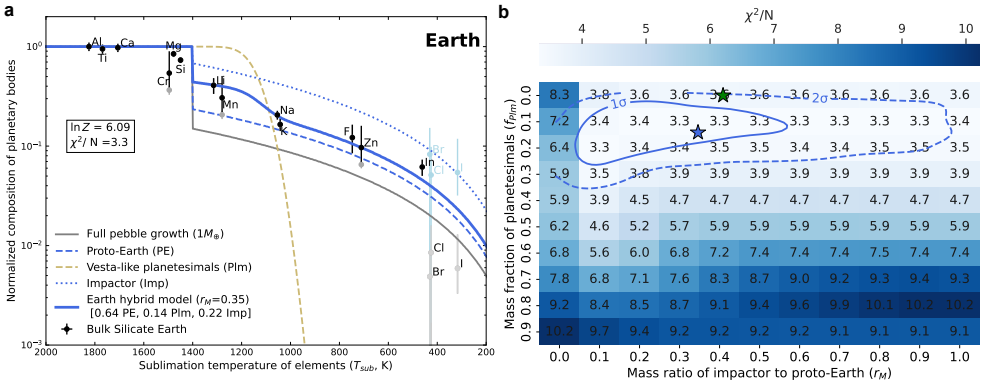


Fig. 3: **Volatile depletion reveals hybrid accretion of Earth.** (**a**) Earth's volatile depletion pattern (solid curve in blue) resulting from the median (central-estimate) solution ([0.64 **PE**, 0.14 **Plm**, 0.22 **Imp**]) of the Bayesian inference of the model combining proto-Earth (**PE**, dashed curve in blue) and Impactor (**Imp**, dotted curve in blue) that grew via pebble accretion, together with a population of Vesta-like planetesimals (**Plm**, dashed curve in yellow). The solution is constrained by the protosolar- and Al-normalized composition of major rock-forming lithophile elements (dots in black) in Earth as a function of elemental sublimation temperature (Extended Data Table 1). The Bayesian evidence (ln Z) and (post-calculated) reduced-χ^2 (χ^2/N, where N is the number of major rock-forming lithophile elements adopted for the inference, 13 in total) are shown in the box for reference (see Fig. 4a for the posterior distributions). Lithophiles with a suspected moderately siderophile or chalcophile tendency (here Cr, Mn, and Zn) have been corrected with a uniform partition coefficient between core and mantle of 1^{+2}_{-1} (while uncorrected values are shown in gray; see our sensitivity tests of this correction in Supplementary Fig. 1a; Supplementary Information). Heavy halogens (Cl, Br and I) are not included in the inference, due to their disputed abundances in CI chondrites (with two sets of data shown in gray and light blue, respectively; Methods). (**b**) Color-coded grid of the reduced-χ^2 as a function of the mass ratio of impactor to proto-Earth (r_M) and the mass fraction of planetesimals ($f_{\rm Plm}$). It is superimposed by the 1σ and 2σ contours of the posterior distributions of the Bayesian inference of the **PE+Plm+Imp** model. The central-estimate solutions of the two most favorable scenarios for Earth's hybrid accretion (**PE+Plm+Imp** and **PE+Imp**; Table 1) are denoted by star signs in blue and green, respectively.

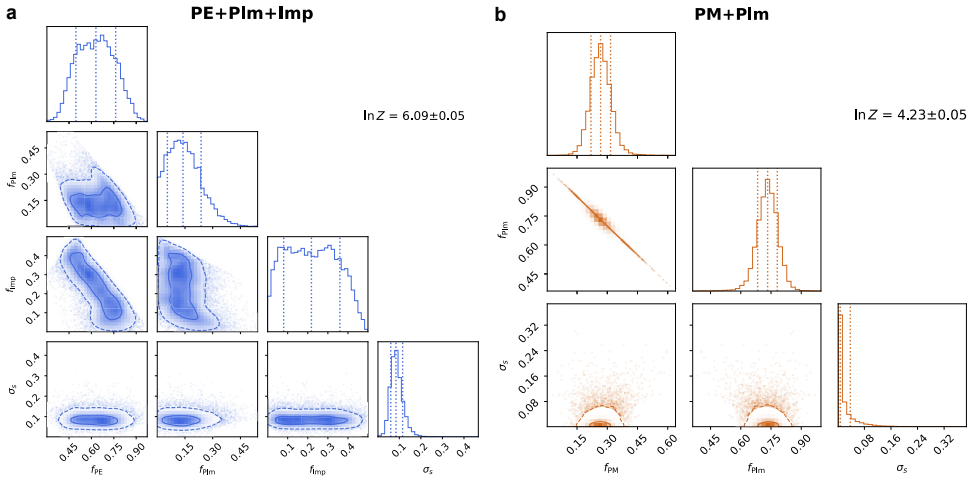


Fig. 4: **Bayesian posterior distributions of formation model parameters for Earth and Mars.** Panels a and b respectively represent their reference models: **PE+Plm+Imp** (Earth) and **PM+Plm** (Mars). The model parameters consists of individual component fractions (f) and an inference intrinsic scatter (σ_s). The 1σ- and 2σ-contours are shown in solid and dashed curves on each corner. On the 1D-histograms of individual parameters along the diagonal panels, the [16th, 50th, 84th] percentiles are shown in dotted lines. The Bayesian evidence ($\ln Z$) with 1σ uncertainty is also shown for each case.

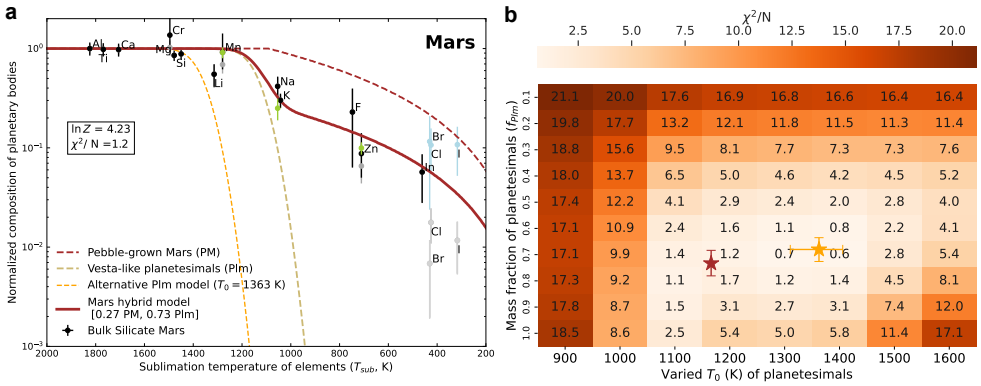
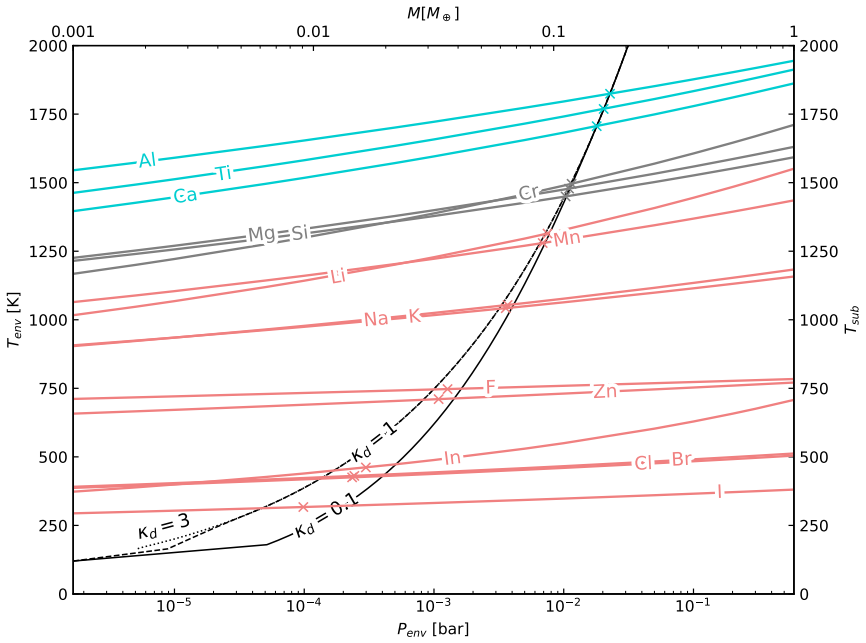


Fig. 5: **Volatile depletion reveals hybrid accretion of Mars.** (**a**) Mars' volatile depletion pattern (solid curve in red) resulting from the median (central-estimate) solution ([0.27 **PM**, 0.73 **Plm**]) of the Bayesian inference of the model combining a pebble-grown Mars component (**PM**, dashed curve in red) and a population of Vesta-like planetesimals (**Plm**, dashed curve in yellow). An alternative planetesimal model of higher T_0 is shown for comparison. The Bayesian evidence ($\ln Z$) and (post-calculated) reduced-χ^2 are shown for reference (see Fig. 4b for the posterior distributions). Similar to Earth's case, the abundances of Cr, Mn, and Zn are corrected for their potential partition into the core (with the same assumption of partition coefficient, $D = 1^{+2}_{-1}$; the uncorrected values are shown in gray; see our sensitivity tests of this correction in Supplementary Fig. 1b; Supplementary Information). Heavy halogens (Cl, Br and I) with disputed CI chondritic abundances are, as for Earth, not included in the inference. The recent update of the Martian mantle composition [60] is consistent within error bars of [3], with major differences mainly for Mn, Na and Zn (the values of those major updates are shown in green for comparison). (**b**) Color-coded grid of reduced-χ^2 as a function of the inflection point (T_0) of a logistic model of volatile-depleted planetesimals (x-axis) and of the relative mass contribution of such planetesimals ($f_{\rm Plm}$; y-axis). For guidance, $f_{\rm Plm}$ (=0.73±0.05) for the reference model (panel A) with a Vesta-like composition (with $T_0 = 1135 \pm 35$ K) is shown in the star sign (with error bars) in brown. Given a varied T_0 (and thus varied volatile depletions) of early-formed planetesimals, the alternative solution is found at $T_0 = 1363^{+43}_{-52}$ K and $f_{\rm Plm} = 0.68 \pm 0.05$ (the star sign with error bars in orange; for more details see Table 1 and Extended Data Fig. 7 and Supplementary Fig. 6)

Table 1: Summary of Bayesian inference results of various hybrid-accretion scenarios of both Earth and Mars.

	Model	$[f_0, ..., f_i]$	χ^2/N	$\ln Z$	$\Delta \ln Z$
Earth	**PE+Plm+Imp**	$[0.64^{+0.12}_{-0.14}, 0.14^{+0.10}_{-0.09}, 0.22^{+0.14}_{-0.15}]$	3.3	6.09 ± 0.05	Reference
	PE+Imp	$[0.71 \pm 0.14, 0.29 \pm 0.14]$	3.6	6.16 ± 0.04	0.07 ± 0.06
	PE+Plm	$[0.73 \pm 0.11, 0.27 \pm 0.11]$	5.9	4.78 ± 0.05	-1.31 ± 0.07
	CI+Plm	$[0.12^{+0.10}_{-0.08}, 0.88^{+0.08}_{-0.10}]$	11.2	-5.22 ± 0.05	-11.31 ± 0.07
	PE+CI+Plm	$[0.74^{+0.09}_{-0.10}, 0.06 \pm 0.04, 0.20^{+0.11}_{-0.10}]$	3.6	4.02 ± 0.06	-2.07 ± 0.07
	PE+CI+Plm+Imp	$[0.66^{+0.11}_{-0.16}, 0.03^{+0.04}_{-0.02}, 0.12^{+0.10}_{-0.08}, 0.19^{+0.08}_{-0.15}]$	3.9	4.31 ± 0.06	-1.78 ± 0.08
	PE+Plm+DualImp	$[0.61^{+0.13}_{-0.15}, 0.10^{+0.09}_{-0.07}, 0.25^{+0.11}_{-0.15}, 0.04^{+0.08}_{-0.03}]$	3.8	5.55 ± 0.05	-0.54 ± 0.06
	PE+Plm+TriImp	$[0.60^{+0.12}_{-0.16}, 0.08^{+0.09}_{-0.06}, 0.25^{+0.09}_{-0.15}, 0.05^{+0.08}_{-0.03}, 0.01^{+0.02}_{-0.01}]$	5.2	4.32 ± 0.06	-1.77 ± 0.07
	PE+Plm+Imp (b^H)	$[0.64^{+0.13}_{-0.15}, 0.14^{+0.11}_{-0.09}, 0.22^{+0.14}_{-0.15}]$	5.9	5.03 ± 0.05	-1.06 ± 0.06
	PE+Plm+Imp ($0.5b^H$)	$[0.64^{+0.13}_{-0.14}, 0.14^{+0.10}_{-0.09}, 0.22^{+0.14}_{-0.15}]$	5.3	5.32 ± 0.05	-0.77 ± 0.06
	PE+Plm+Imp ($0.1b^H$)	$[0.64^{+0.12}_{-0.14}, 0.14^{+0.10}_{-0.09}, 0.22 \pm 0.14]$	3.8	6.01 ± 0.05	-0.08 ± 0.06
Mars	**PM+Plm**	$[0.27 \pm 0.05, 0.73 \pm 0.05]$	1.2	4.23 ± 0.05	Reference
	CI+Plm	$[0.15^{+0.07}_{-0.05}, 0.85^{+0.05}_{-0.07}]$	2.4	0.12 ± 0.05	-4.11 ± 0.06
	PM+CI+Plm	$[0.22^{+0.06}_{-0.07}, 0.03^{+0.04}_{-0.02}, 0.75^{+0.05}_{-0.06}]$	1.3	1.86 ± 0.07	-2.37 ± 0.09
	PM+Plm (var. T_0)	$[0.32 \pm 0.05, 0.68 \pm 0.05]$	0.6	5.52 ± 0.06	1.29 ± 0.08
	PM+Plm (var. T_0&σ_0)	$[0.21^{+0.09}_{-0.11}, 0.79^{+0.11}_{-0.09}]$	0.2	6.81 ± 0.07	2.58 ± 0.09

Notation $[f_0, ..., f_i]$ represents the relative mass fractions (with 50th percentile as the median and 16th–84th percentiles as the error bars) of accreted components of a planet, listed in the same order as their appearance in the named models – e.g., **PE** (proto-Earth)+**Plm** (Planetesimals)+**Imp** (Impactor) as the reference model for Earth and **PM** (pebble-grown Mars component)+**Plm** as the reference model for Mars. **CI** represents a population of volatile-rich CI-like planetesimals. **DualImp** and **TriImp** represent dual and triple impactors, respectively. b^H, $0.5b^H$, and $0.1b^H$ indicate different levels of pre-depletion of accreted pebbles (Methods). Please refer to Methods for calculation details of the reduced-χ^2 (χ^2/N) and of Bayesian inference including the logarithmic Bayesian evidence ($\ln Z$) and Bayes factor ($\Delta \ln Z = \ln Z - \ln Z_{\rm ref}$, where 'ref' denotes the adopted reference model correspondingly), as well as the definitions of T_0 and σ_0 of the adopted volatile-depleted planetesimal model.



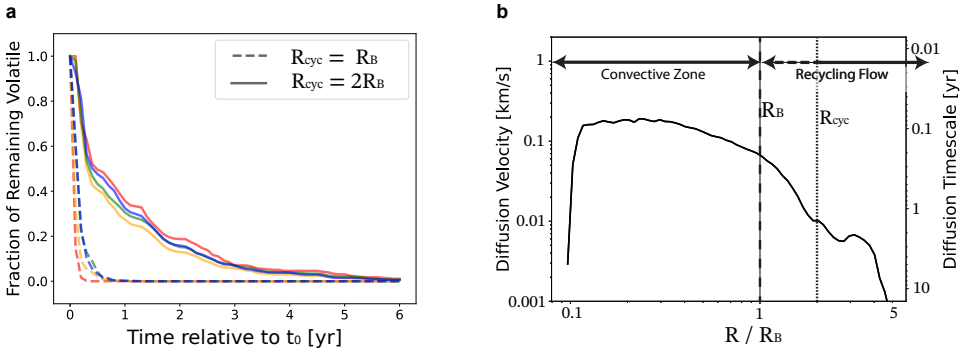
Extended Data Fig. 1: **The pressure ($P_{\rm env}$)–temperature ($T_{\rm env}$) profiles at the bottom of the envelope of the pebble-accreting body over its growth**, along with the pressure-dependent elemental sublimation temperatures ($T_{\rm sub}$; Extended Data Table 1), for two different opacity conditions in the surrounding protoplanetary disk ($\kappa_{\rm d} = [0.1,\, 1]\,{\rm m^2\,kg^{-1}}$). The adopted mean $T_{\rm sub}$ values are denoted by cross ('×') signs. The dotted curve shows that a further increase of the opacity parameter ($\kappa_{\rm d}$) by a factor of 3 over the unity value (resulting, for example, from release of dust and recondensed MVLEs from the pebbles) will not change the bottom $P_{\rm env}$–$T_{\rm env}$ profile significantly and thus the elemental sublimation temperatures are robust to opacity changes.

Extended Data Table 1: **Elemental sublimation temperatures ($T_{\rm sub}$) for different disk opacity conditions ($\kappa_{\rm d} = [0.1, 1]\,{\rm m^2\,kg^{-1}}$) as well as their mean values (with negligible error bars) that are adopted for model exploration.** Corresponding to those $T_{\rm sub}$ values at the limits of the opacity range, the specific pressures ($P_{\rm sub}$) at which $T_{\rm sub}$ values are interpolated from the recommended pressure-dependent $T_{\rm c}^{50}$ (equivalent to $T_{\rm sub}$ here) model [8] ($10^4/T_{\rm c}^{50} = \alpha \log_{10} P({\rm bar}) + \beta$, where our best-fit values of α and β) are specified in the last two columns for reference). Note that the $T_{\rm sub}$ values for light halogens Cl, Br and I are only used for plotting but not for model fitting. S is not included for model fitting either, but its $T_{\rm sub}$ is used to infer the nominal S composition from the best-solution models of hybrid accretion.

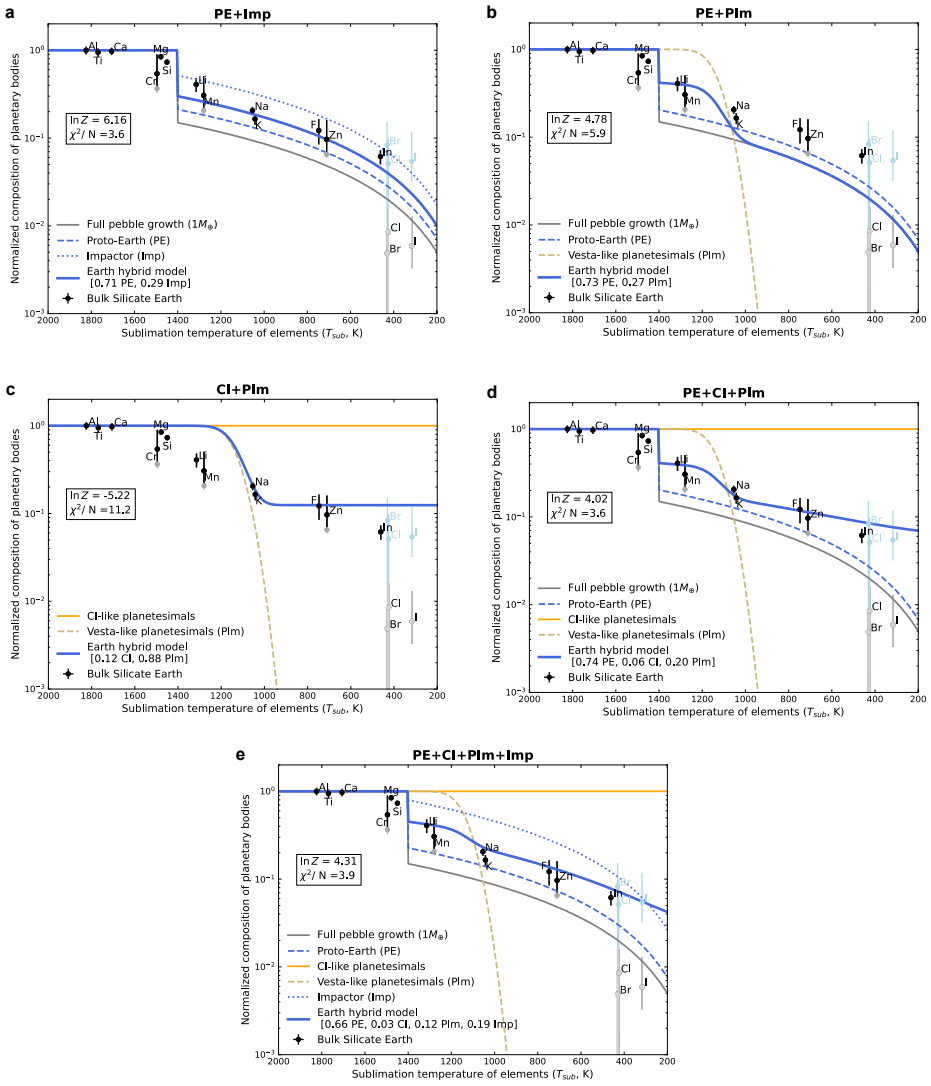
X	$\kappa_d = 0.1\,,{\rm m^2\,kg^{-1}}$		$\kappa_d = 1\,{\rm m^2\,kg^{-1}}$		$\overline{T_{\rm sub}}$, K	Best-fit parameters	
	$T_{\rm sub}$, K	$P_{\rm sub}$, bar	$T_{\rm sub}$, K	$P_{\rm sub}$, bar		α	β
Al	1824	2.3×10^{-2}	1824	2.3×10^{-2}	1824	-0.2395	5.0883
Ti	1769	2.0×10^{-2}	1769	2.0×10^{-2}	1769	-0.2896	5.1634
Ca	1706	1.8×10^{-2}	1706	1.8×10^{-2}	1706	-0.3230	5.2976
Mg	1479	1.1×10^{-2}	1477	1.1×10^{-2}	1478	-0.3650	6.0502
Si	1450	1.1×10^{-2}	1449	1.0×10^{-2}	1450	-0.3519	6.1664
Cr	1496	1.2×10^{-2}	1495	1.1×10^{-2}	1496	-0.4903	5.7343
Li	1316	7.8×10^{-3}	1312	7.2×10^{-3}	1314	-0.6108	6.3101
Mn	1281	7.2×10^{-3}	1278	6.6×10^{-3}	1280	-0.4375	6.8678
Na	1056	4.1×10^{-3}	1051	3.3×10^{-3}	1054	-0.4706	8.3443
K	1045	4.0×10^{-3}	1040	3.2×10^{-3}	1042	-0.4308	8.5403
F	749	1.6×10^{-3}	746	9.9×10^{-4}	747	-0.2346	12.7031
Zn	713	1.4×10^{-3}	708	8.2×10^{-4}	711	-0.4028	12.8792
In	473	5.1×10^{-4}	450	1.7×10^{-4}	461	-2.2867	13.6120
Br	435	4.2×10^{-4}	426	1.4×10^{-4}	431	-1.0928	19.2740
Cl	430	4.0×10^{-4}	420	1.3×10^{-4}	425	-1.0857	19.5766
I	321	2.0×10^{-4}	313	4.8×10^{-5}	317	-1.3935	25.9576
S	661	1.2×10^{-3}	661	6.5×10^{-4}	661	0.0	15.1286

Extended Data Table 2: A set of priors applied to perform the Bayesian inference

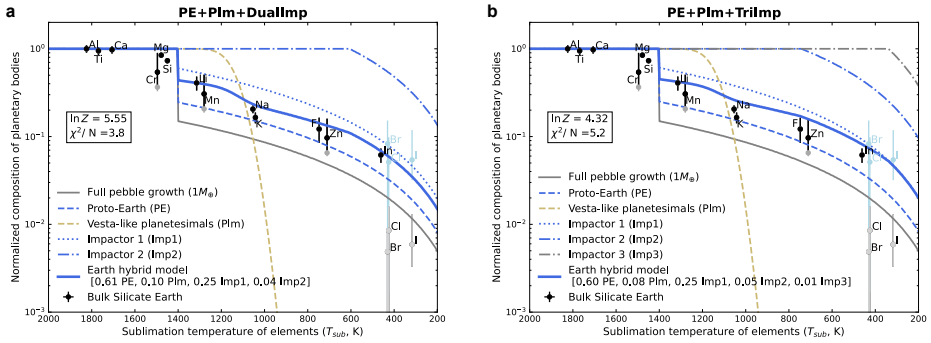
Parameter	**Prior Condition**	**Description**
Fraction (f)	$\mathcal{U}[0,1]$ & $\sum_i f_i = 1$	Following the Dirichlet prior, i.e., fraction of each component (f_i) is within 0–1 (uniform) and their sum is equal to 1.
Fraction (f)	$f_{\rm Imp} \leq f_{\rm pp}$	Where applicable, the fraction of an impactor ($f_{\rm Imp}$) is no greater than that of the protoplanet ($f_{\rm pp}$).
Fraction (f)	$f_{\rm Imp}^{i+1} \leq f_{\rm Imp}^{i}$	Where applicable, the fraction of a subsequent impactor ($f_{\rm Imp}^{i+1}$) is no greater than that of the preceding one ($f_{\rm Imp}^{i}$).
Scatter (σ_s)	$\mathcal{U}[10^{-3}, 10^{1}]$	A broad bound of the intrinsic scatter (uniform).
T_0 (K)	$\mathcal{U}[500, 2000]$	Where applicable, a broad bound of the inflection point (T_0) of a planetesimal logistic model (uniform).
σ_0 (K)	$\mathcal{U}[10, 500]$	Where applicable, a broad bound of the steepness (σ_0) of a planetesimal logistic model (uniform).



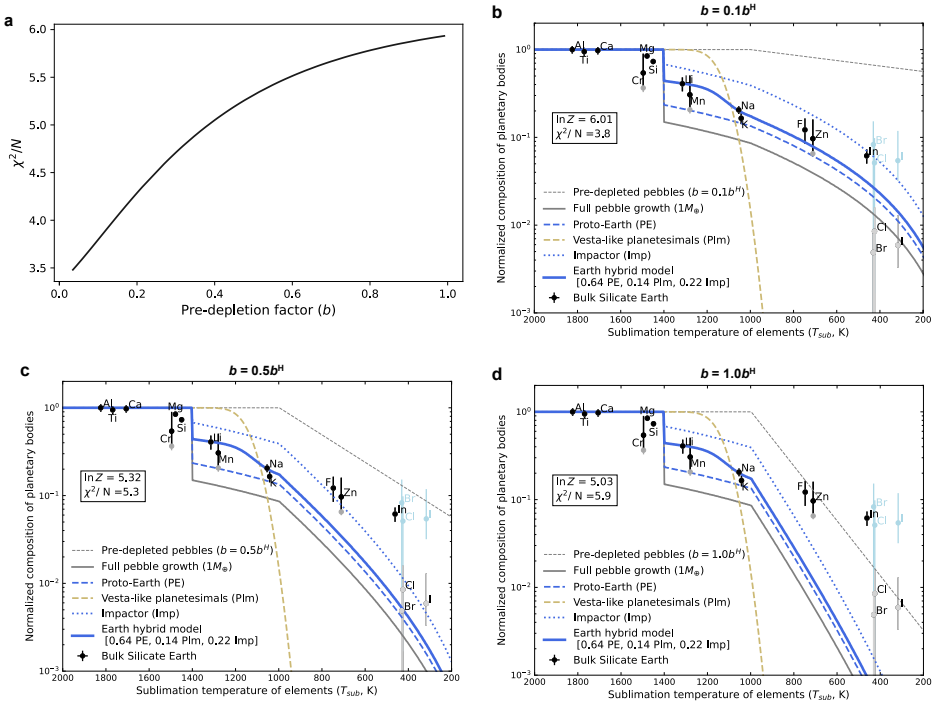
Extended Data Fig. 2: **The effect of different assumptions of the recycling range $R_{\rm cyc}$ on diffusion timescale of particles.** (**a**) The surviving particle fraction as a function of time for two values of $R_{\rm cyc}$ and for different spatial intervals of particles initially placed in the envelope: 0.1-0.3 $R_{\rm B}$ (red), 0.3-0.6 $R_{\rm B}$ (yellow), 0.6-0.8 $R_{\rm B}$ (green), and 0.8-1 $R_{\rm B}$ (blue). We note that for our assumed two values of $R_{\rm cyc}$, the case of $R_{\rm cyc} \approx R_{\rm B}$ is the most realistic [43], but loss of volatiles is rapid under both assumptions. (**b**) The measured diffusion velocity and diffusion time-scale as a function of distance from the outgassed atmosphere of the protoplanet. The reduction in the strength of the convection in the convective overshoot region beyond $R_{\rm B}$ is clearly visible.



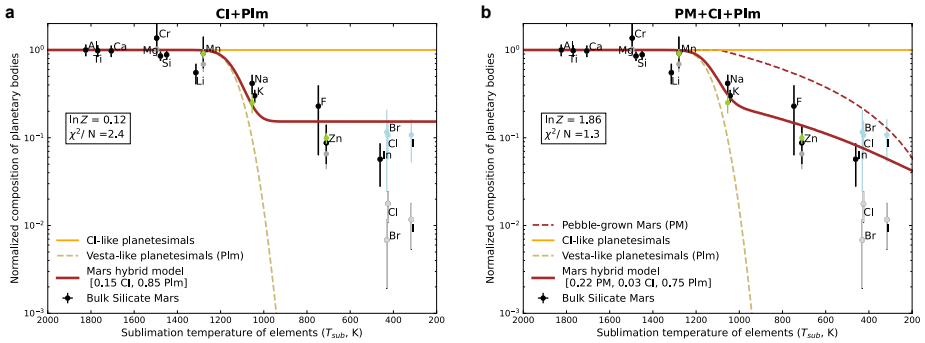
Extended Data Fig. 3: **Tests of the essentiality of potential components (PE, Plm, Imp, CI) for Earth's accretion.** (**a**) The **PE+Imp** model. (**b**) The **PE+Plm** model. (**c**) The **CI+Plm** model. (**d**) The **PE+CI+Plm** model. (**e**) The **PE+CI+Plm+Imp** model. We refer to Fig. 3 for notations and Supplementary Fig. 3 for corresponding posterior distributions of the Bayesian inferences.



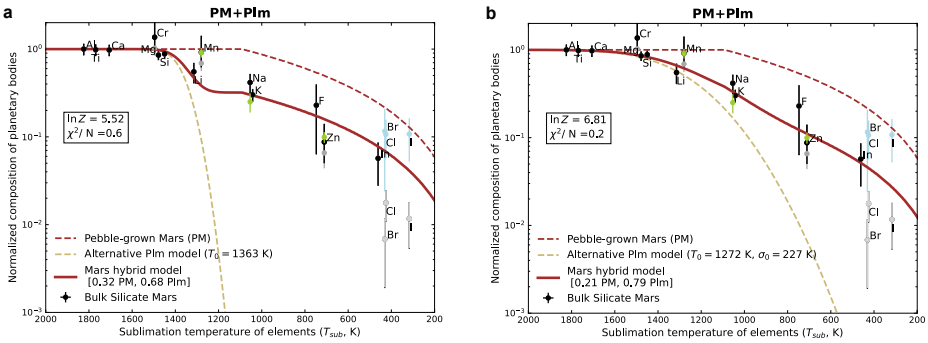
Extended Data Fig. 4: **Tests of multi-impactor scenarios for Earth's accretion.** (**a**) The **PE+Plm+DualImp** model. (**b**) The **PE+Plm+TriImp** model. We refer to Fig. 3 for notations and Supplementary Fig. 4 for corresponding posterior distributions of the Bayesian inferences.



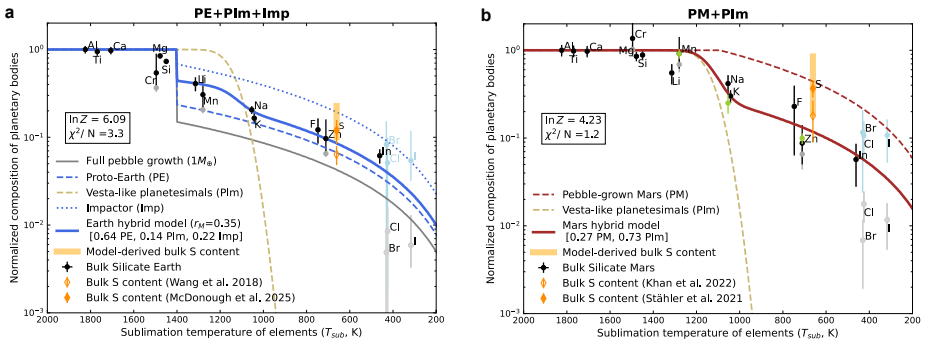
Extended Data Fig. 5: **Tests of pre-depleted pebbles for Earth's accretion**. (**a**) The reduced-χ^2 (χ^2/N) as a function of pre-depletion factor (b), which is relative to the depletion slope of H-chondrite model ($b^{\mathrm{H}} = -3.12$; Methods). (**b**) The case of $b = 0.1b^{\mathrm{H}}$. (**c**) The case of $b = 0.5b^{\mathrm{H}}$. (**d**) The case of $b = 1.0b^{\mathrm{H}}$. We refer to Fig. 3 for notations.



Extended Data Fig. 6: **Tests of the essentiality of a volatile-rich CI-like component (CI) for Mars's accretion.** (**a**) The **CI+Plm** model. (**b**) The **PM+CI+Plm** model. We refer to Fig. 5 for notations and Supplementary Fig. 5 for corresponding posterior distributions of the Bayesian inferences.



Extended Data Fig. 7: **Tests of varied T_0 and/or σ_0 of the logistic model of volatile-depleted planetesimals (in the case of Mars)** (**a**) The **PM+Plm (varied T_0)** model. (**b**) The **PM+Plm (varied T_0&σ_0)** model. We refer to Fig. 5 for notations and Supplementary Fig. 6 for corresponding posterior distributions of the Bayesian inferences.



Extended Data Fig. 8: **Model-derived sulfur (S) contents in bulk Earth and Mars based on the best-solutions of the reference hybrid-accretion models (PE+Plm+Imp and PM+Plm) of Earth and Mars (yellow bars).** (**a**) The result for bulk Earth compared to two different estimates in the literature (yellow diamonds). (**b**) The result for bulk Mars compared to two different estimates in the literature (yellow diamonds). For the Khan et al. estimate, we have adopted their calibrated uppermost and lowermost limits of core S content (3.1–9.1 wt%), while using the same core mas fraction (0.25 ± 0.005) as of Stähler et al. to convert to bulk S content in Mars.

Supplementary Files

This is a list of supplementary files associated with this preprint. Click to download.

- PebbledevolatilizationNatAstroR2Suppl.pdf